

Supporting Information for

High Capacity/Reversible Fe/Sn Alloy for Na-storage Anode Enabled by Thermal Reaction then Anchored on Exfoliated Graphite

Tianbiao Zeng, Xinxin Zhu, Xintong Wang, Lichen Zhang, Yihong Ding*, Huile Jin

Key Laboratory of Carbon Materials of Zhejiang Province, Wenzhou Key Lab of Advanced Energy Storage and Conversion, Zhejiang Province Key Lab of Leather Engineering, College of Chemistry and Materials Engineering, Wenzhou University, Wenzhou Zhejiang 325035, China.

*: Corresponding authors. Email: yhdd@wzu.edu.cn

Table S1 The energy of some Fe-Sn alloy, FeS_y, SnS₂ and SnS

Materials	Fe	Fe ₁₁ S ₁₂	Fe ₂ S	Fe ₂ Sn	Fe ₃ S	Fe ₃ S ₄
Crystal ID	mp-13	mp-1225858	mp-851357	mp-510164	mp-1184373	mp-850016
Energy eV/atom	-8.3058	-6.5385	-6.9766	-6.4896	-7.0316	-6.3155
Materials	Fe ₄ S ₅	Fe ₇ S ₁₂	Fe ₇ S ₈	FeS ₂	FeSn	FeSn ₂
Crystal ID	mp-850083	mp-684707	mp-556435	mp-1522	mp-21260	mp-22752
Energy eV/atom	-6.5055	-6.0008	-6.5226	-6.0781	-6.0618	-5.3959
Materials	Fe ₃ Sn	Fe ₃ Sn ₂	Sn	SnS	SnS ₂	FeS
Crystal ID	mp-22461	mp-27505	Mp-117	mp-2231	mp-1170	mp-505531
Energy eV/atom	-6.8411	-6.4633	-3.9746	-4.5144	-4.4623	-6.8030

Theoretical Calculation and Experimental

1. Theoretical calculation

The theoretical calculations were performed using VASP software and visualized all the structures on VESTA software. For first-principles calculations based on density functional theory (DFT), standard crystallographic information files (CIFs) downloaded from the website of Materials

Project, and structures for molecular dynamic (MD) simulation were constructed according to the actual situation. Before energy and band structure calculations, all structures were geometry optimized. The Perdew-Burke-Ernzerhof exchange-correlation function within the generalized gradient approximation (GGA-PBE) method was employed to describe the electronic exchange-correlation effects.¹ The cut-off energy was 520 eV, the convergence criterion was 1×10^{-4} eV, and the primitive cells and $5 \times 5 \times 5$ k-point mesh were applied for free energy calculations. For band structure calculation, the HSE06 method was employed with a k-point mesh resolution of 0.06 eV for the self-consistent field (SCF) calculation, and a k-point mesh resolution value of 0.06 eV was used along the K-path.^{2, 3} In the MD simulation, the Gamma point was applied as the K-point set. The Na⁺ diffuse coefficient was determined by the following equation based on MD simulation:^{4, 5}

$$D_{Na^+} = \lim_{t \rightarrow \infty} \frac{\langle r^2(t) \rangle}{6dt}$$

Here, $\langle r^2(t) \rangle/t$ is the slope of the mean square displacement (MSD) of the Na atom.

The work function was computed using the following equation:⁶

$$E_w = E_v - E_F$$

The E_v is the surface vacuum energy level of an electron within a specific structure, while E_F is the Fermi level of the electron in the aforementioned structure.

2. Synthesis of materials

SnS₂, Fe, and graphite powder were supplied by Shanghai Aladdin Reagent Co., Ltd., and utilized directly without further treatment. Briefly, Fe and SnS₂ were weighed in mole ratios of 1:1 and mixed, then loaded 2.00 g mixed powder to a quartz tube of 10 cm in length, 10.0 mm outer diameter, and 1.0 mm in thickness, the tube was then evacuated until the pressure lower than 10 Pa, then sealed, and heated to 600 °C at a temperature increase rate of 5 °C/min, and maintaining at 600 °C for 48 h. After heating finished and cooling down to room temperature, a black powder was obtained. The yield black

powder denoted to FSS-1. The FSS-1 was mixed with 15 wt.% graphite and ball milling for 6 h at 800 rpm in an N₂ filled, 50 mL stainless steel ball mill tank. The ball-milled powder denoted to FSS-1/G-15%. The Fe and SnS₂ were adjusted to 2: 1 and 3: 1 mole ratios, and repeat the experiment with the same protocol. The yield products denoted to FSS-2, FSS-2/G-15%, FSS-3, and FSS-3/G-15%, respectively.

3. Characterization

Shimadzu-XRD-7000 X-ray diffractometer was applied to analyze the phase of the synthesized materials (XRD, Cu-K α , 40 kV, 30 mA). Field emission scanning electron microscopy (SEM) of Nova 200 NanoSEM was applied to examine the morphology and structure of the samples and the electrodes, and transmission electron microscopy (TEM) of JEM-2100F was applied to study the fine structure of the samples and the elementals distribution. X-ray photoelectron spectroscopy (XPS) was acquired on Axis Ultra DLD, the specific surface area was evaluated on an Autosorb IQ automated gas absorption analyzer.

The Na-storage performances were investigated on CR2032 coin cells. The samples were mixed with acetylene black and carboxymethylcellulose sodium in a weight ratio of 8:1:1, then adding a small amount of deionized water and stirred for 2 hours to form a slurry, the slurry was then coated onto Cu foil and dried. The foil was punched into 12 mm discs to serve as electrodes, the mass loading was 1.5 \pm 0.2 mg on each disc. The coin cells were assembled within an Ar-filled glove box of H₂O and O₂ lower than 0.5 ppm and 1 ppm. The electrolyte used was a 1 mol/L NaFP₆ solution in a mixture of ethylene carbonate/dimethyl carbonate/propylene carbonate with 1:1:1 volume ratio, and adding 5 wt.% of fluoroethylene as the additive. Whatman GF/D glass paper discs were employed as separators. The cyclic voltammetry (CV) tests were conducted using an EC-100B electrochemical workstation, with a scan rate of 0.1 mV s⁻¹ for the initial 6 scans, followed by 0.2 mV s⁻¹ for 2 scans, 0.4 mV s⁻¹ for 2 scans, 0.6

mV s⁻¹ for 2 scans, 0.8 mV s⁻¹ for 2 scans, and finally 1.0 mV s⁻¹ for 2 scans. The discharge/charge, and galvanostatic intermittent titration technique (GITT) tests were performed on the LAND battery tester. The capacities of all materials are determined by considering the weight of the prepared materials, specifically the FSS-*n* and FSS-*n*/G-15% (where *n*=1, 2, and 3).

The surface pseudocapacitance was determined using B. E. Conway's theory based on the CV scans conducted at rates ranging from 0.2 to 1.0 mV s⁻¹:⁷

$$i(v) = av^b = k_1v + k_2v^{1/2} \quad (1)$$

where *i* is the current (mA), *v* is the scan rate (mV s⁻¹), and *a* and *b* are empirical parameters, *k*₁ and *k*₂ are specific to a given potential. The *b* value corresponds to the capacitance-diffusion factor, in particular, when 0 < *b* ≤ 0.5, the process is primarily diffusion-controlled, while 0.5 < *b* ≤ 1.0 implies the process is dominated by surface capacitive behavior. The terms *k*₁*v* and *k*₂*v*^{1/2} represent the contributions from pseudocapacitance-controlled and diffusion-controlled capacity, respectively.

The Na⁺ diffusion coefficient (*D*_{Na⁺}) was calculated using the following equation:⁸

$$D_{Na^+} = \frac{4}{\pi \cdot \tau} \cdot \left(\frac{m_B \cdot V_m}{M_B \cdot S} \right)^2 \cdot \left(\frac{\Delta E_s}{\Delta E_\tau} \right)^2 \quad (2)$$

where τ is the duration of the current pulse (s), V_m is the molar volume (cm³ mol⁻¹), m_B is the mass loading (g), M_B is the molecular weight (g mol⁻¹), and S is the contact surface area between the electrode and the electrolyte (cm²).

Figures

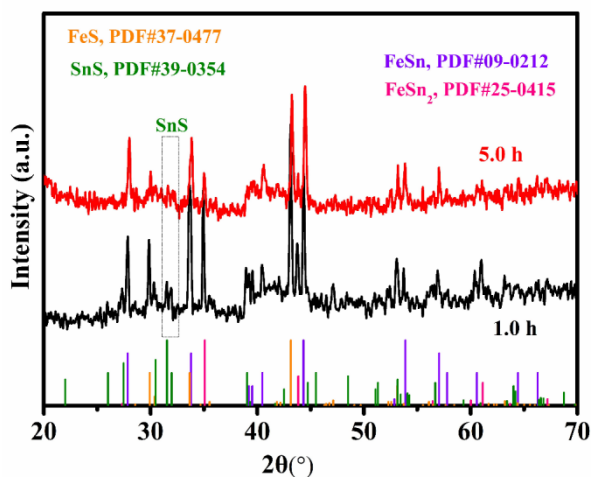


Fig. S1 XRD of heated Fe+SnS₂ powder for 1 h and 5 h in the evacuated quartz tubes, the mole ratio of Fe: SnS₂ = 3:1.

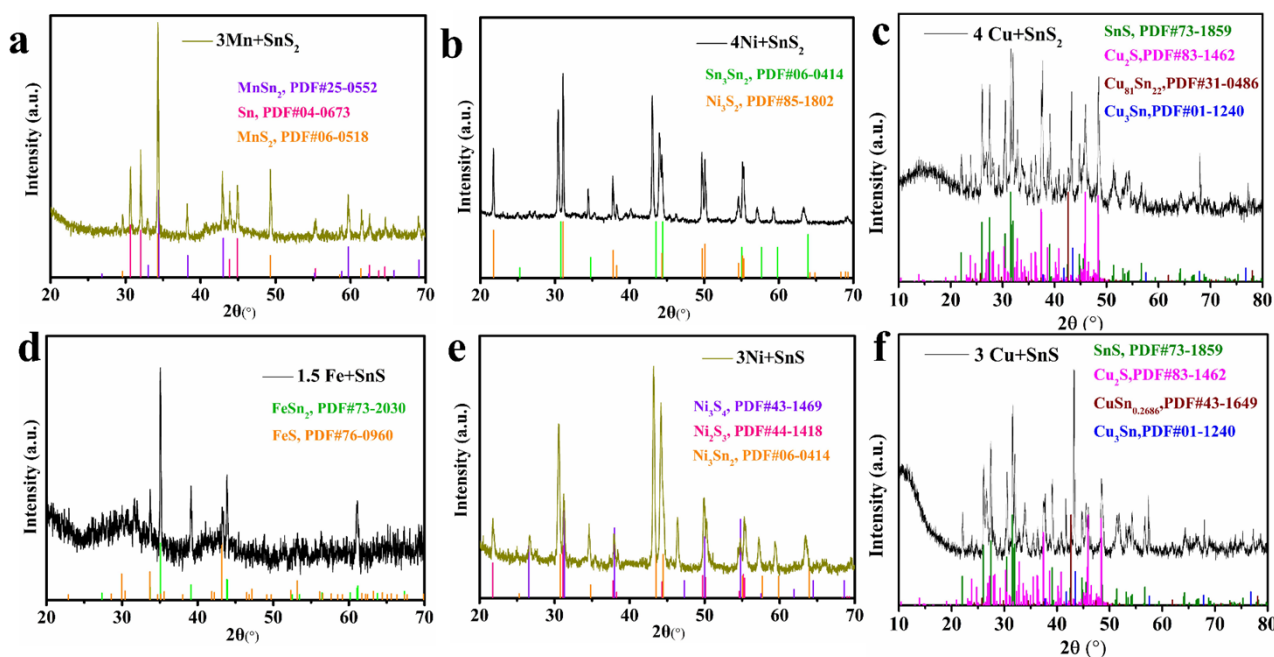


Fig. S2 XRD of heated transition metals with SnS₂ powder. (a) the mole ratio of Mn: SnS₂ = 3:1; (b) the mole ratio of Ni: SnS₂ = 4:1; (c) the mole ratio of Cu: SnS₂ = 4:1; (d) the mole ratio of Fe: SnS = 1.5:1; (e) the mole ratio of Ni: SnS = 3:1; (f) the mole ratio of Cu: SnS = 3:1.

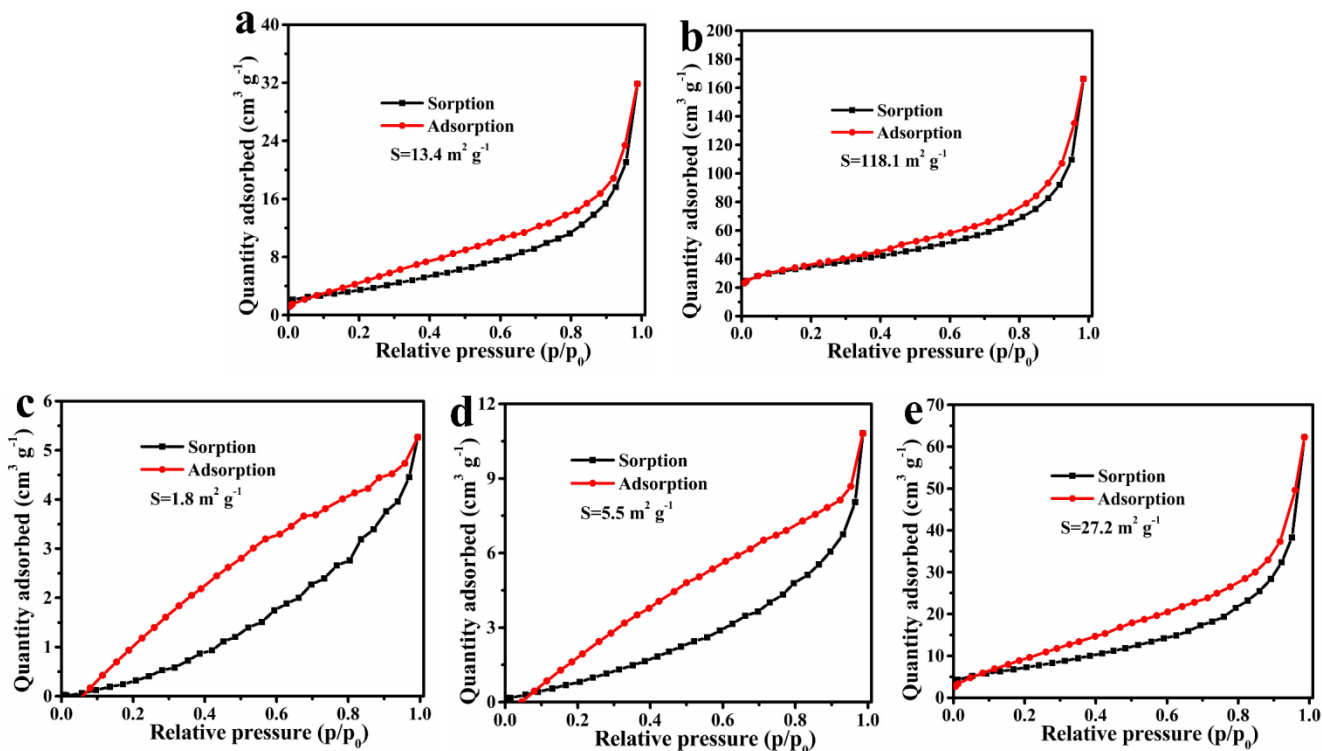


Fig. S3 N₂ adsorption/desorption curve of graphite (a), ball milled graphite (b), FSS-3 (c), ball milled FSS-3 (d), FSS-3/G-15% (e).

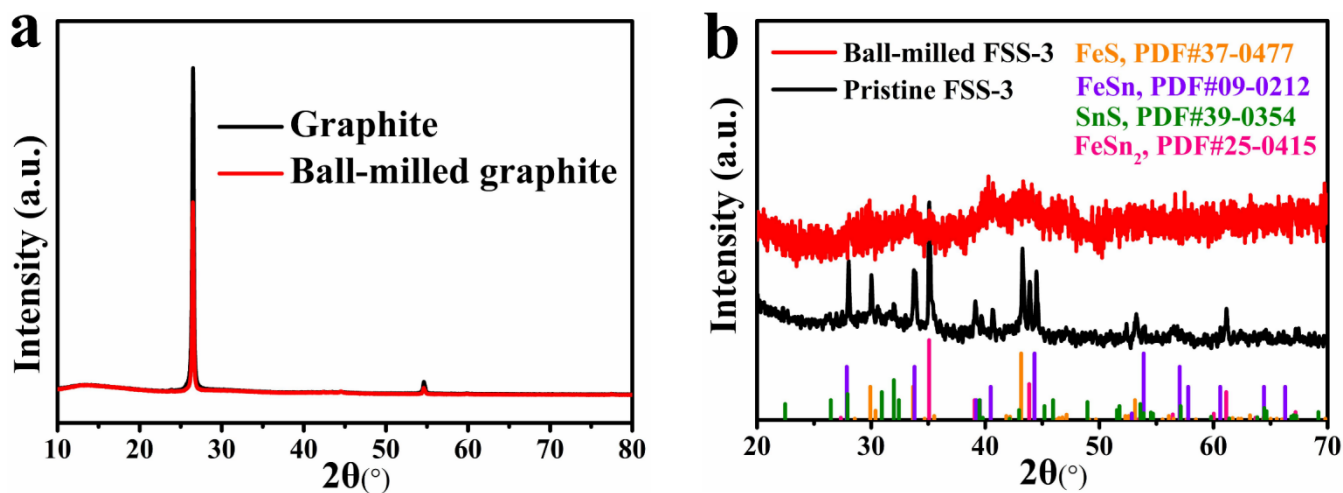


Fig. S4 (a) XRD of graphite and ball-milled graphite, (b) XRD of pristine FSS-3 and ball-milled FSS-3.

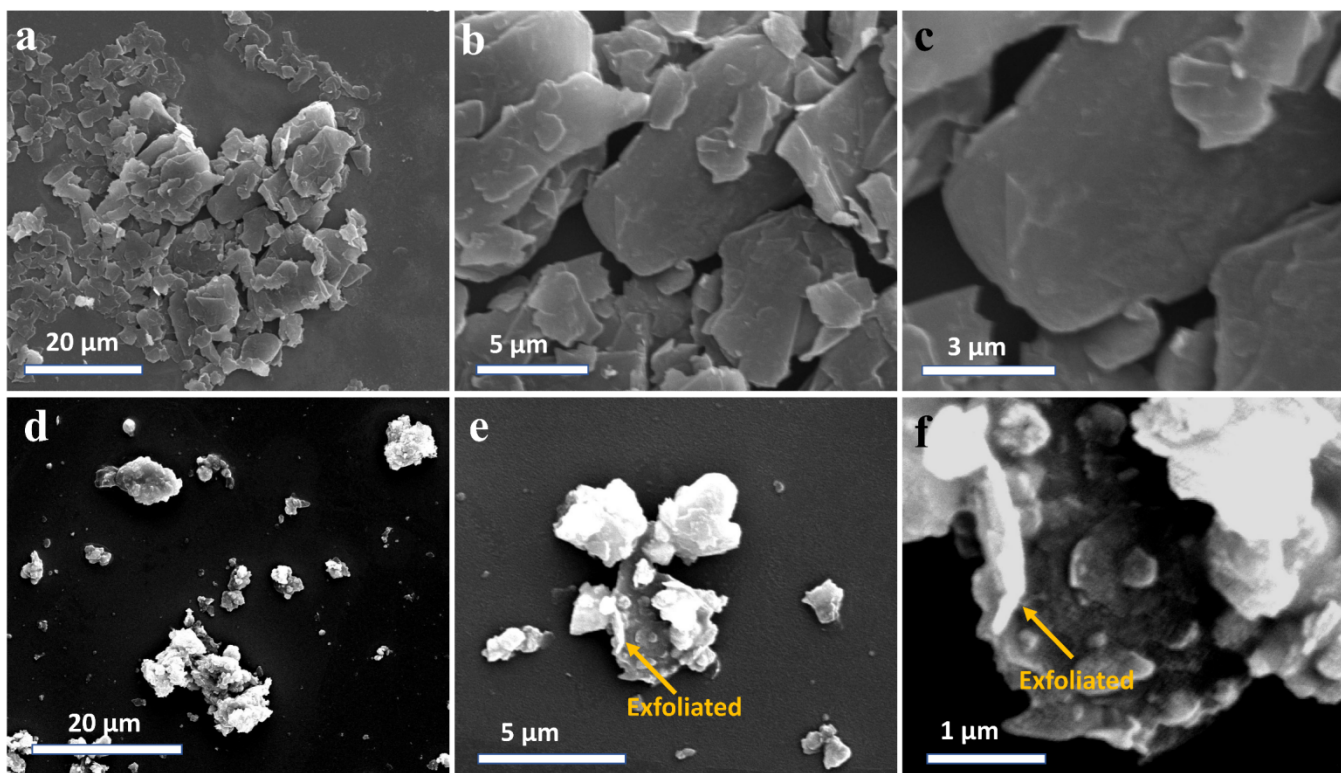


Fig. S5 (a-c) SEM images of pristine graphite, (d-f) the ball-milled graphite.

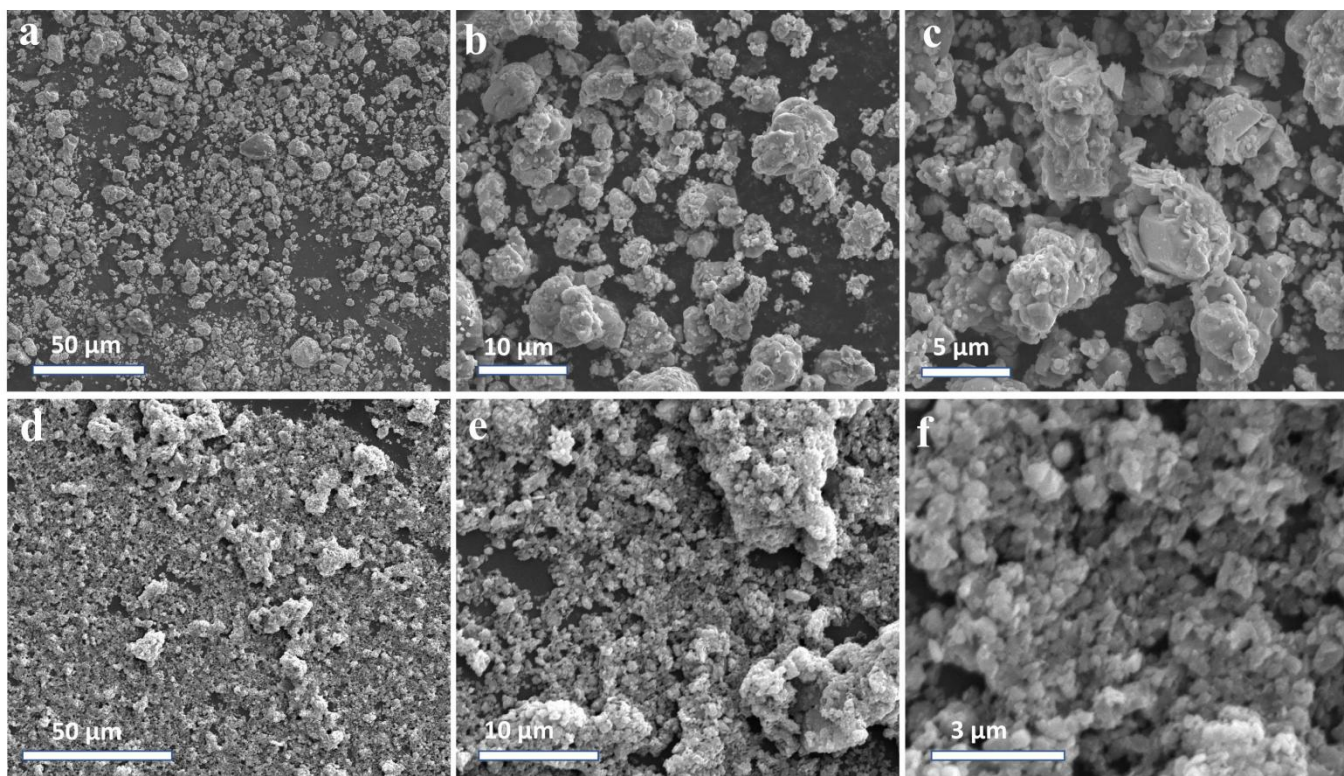


Fig. S6 (a-c) SEM images of pristine FSS-3, (d-f) the ball-milled FSS-3.

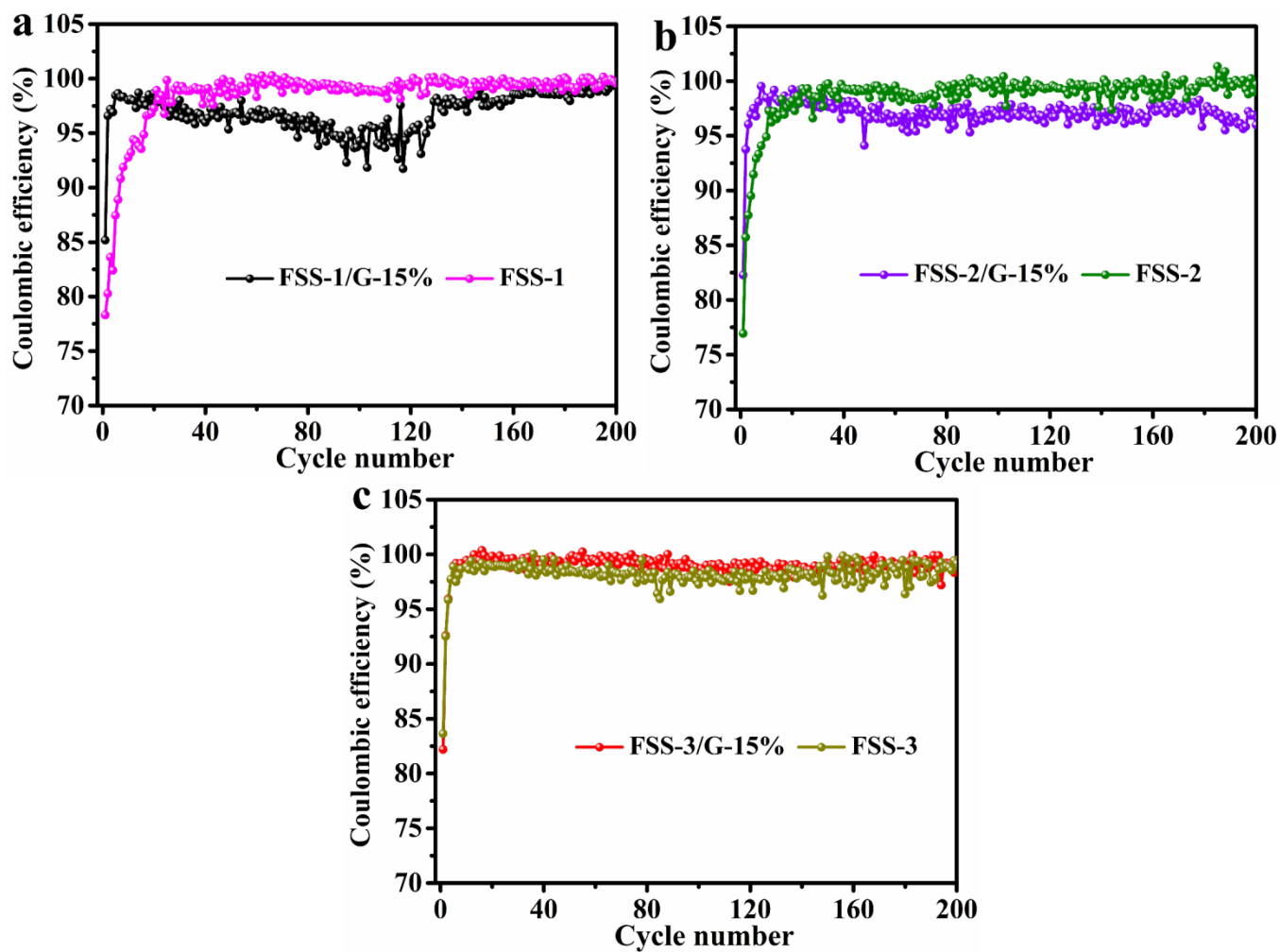


Fig. S7 (a) Charge/discharge coulombic efficiency of FSS-1 and FSS-1/G-15% tested under 0.1 A g^{-1} , (b) charge/discharge coulombic efficiency of FSS-2 and FSS-2/G-15% tested under 0.1 A g^{-1} , (c) charge/discharge coulombic efficiency of FSS-3 and FSS-1/G-15% tested under 0.1 A g^{-1} .

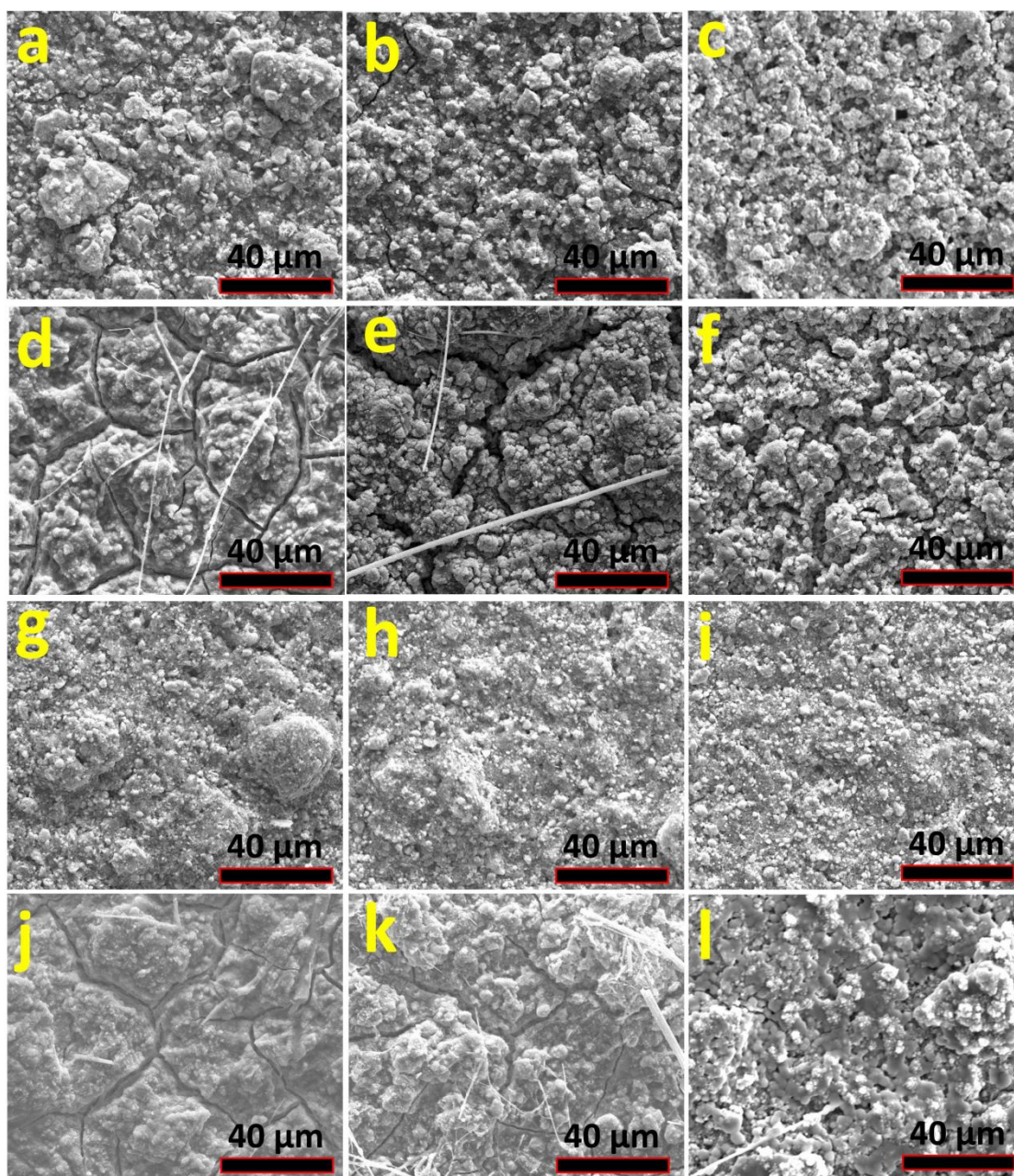


Fig. S8 SEM image of electrodes. (a) pristine FSS-1, (b) pristine FSS-2, (c) pristine FSS-3, (d) the FSS-1 after 100 cycles under 0.1 A g^{-1} , (e) the FSS-2 after 100 cycles under 0.1 A g^{-1} , (f) the FSS-3 after 100 cycles under 0.1 A g^{-1} , (g) pristine FSS-1/G-15%, (h) pristine FSS-2/G-15%, (i) pristine FSS-3/G-15%, (j) the FSS-1/G-15% after 100 cycles under 0.1 A g^{-1} , (k) the FSS-2/G-15% after 100 cycles under 0.1 A g^{-1} , (l) the FSS-3/G-15% after 100 cycles under 0.1 A g^{-1} .

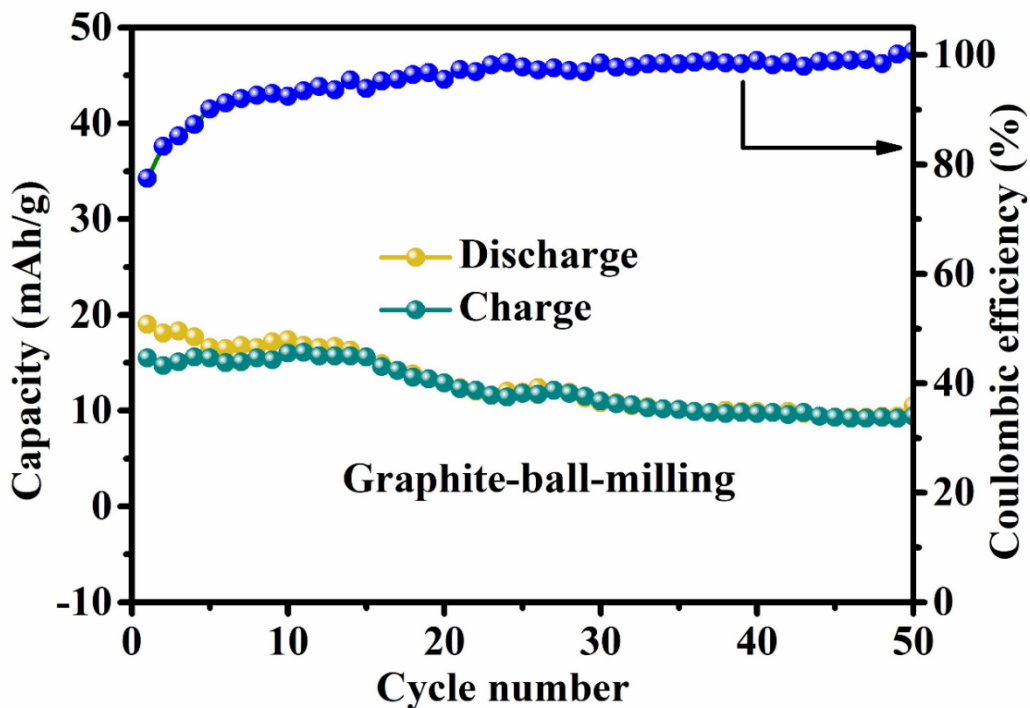


Fig. S9 The cycling performance of exfoliated graphite under 0.1 A g^{-1} .

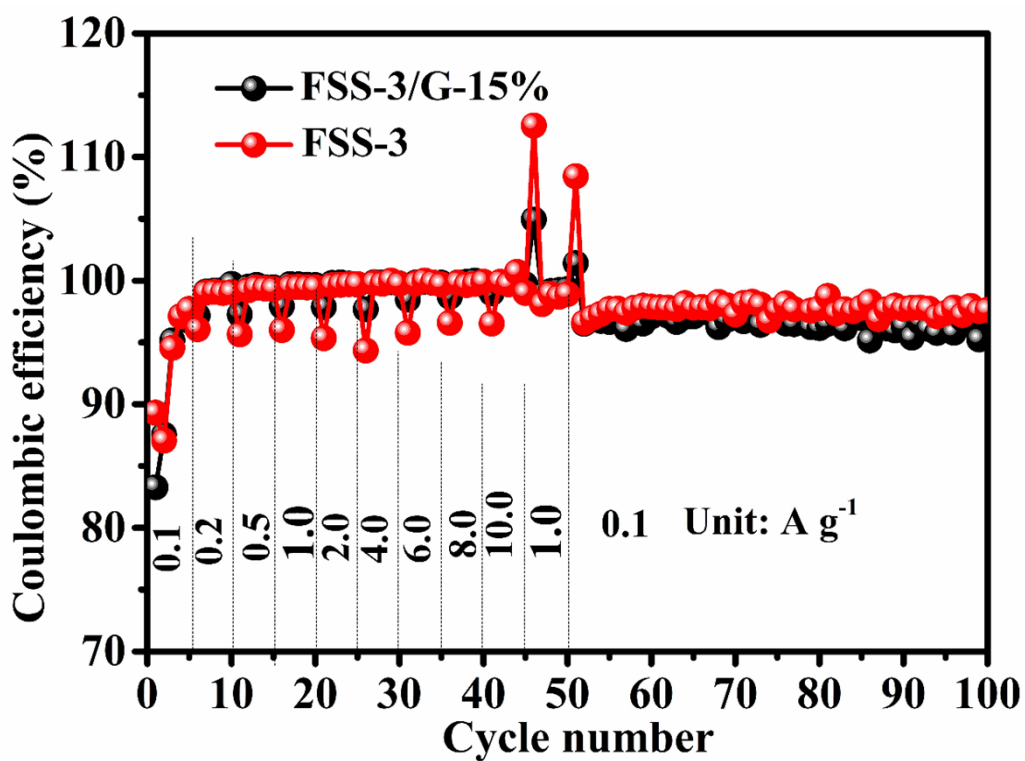


Fig. S10 Coulombic efficiency of FSS-3 and FSS-3/G-15% tested from $0.1 \sim 10.0 \text{ A g}^{-1}$.

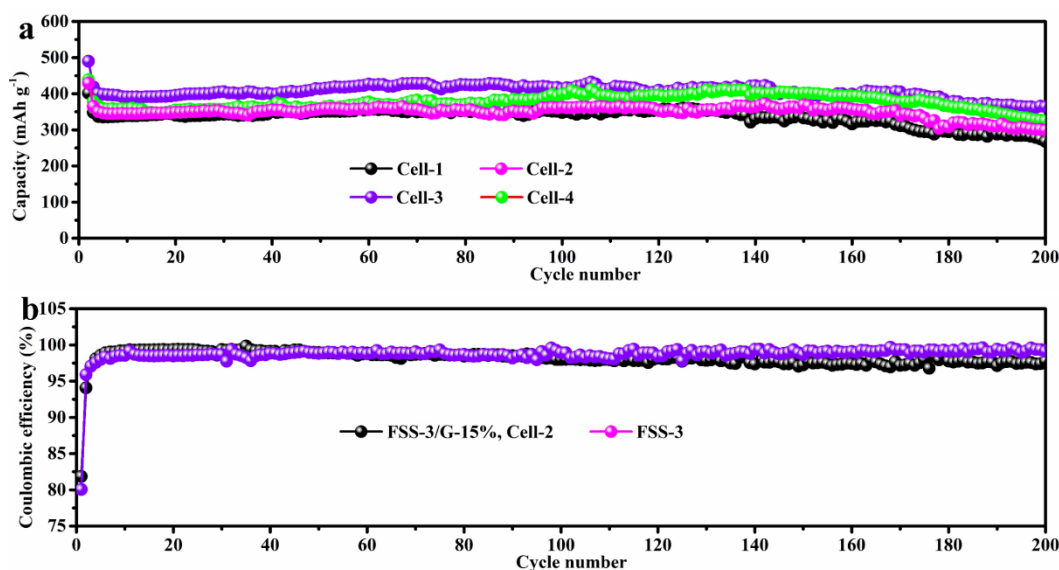


Fig. S11 (a) Galvanostatic discharge/charge capacity of FSS-3/G-15% under 1.0 A g^{-1} , 4 cells was applied to the experiment, and the Cell-2 was used for the main text of Fig. 2g. The stable reversible capacity of FSS-3/G-15% under 1.0 A g^{-1} is about $350\sim 400 \text{ mAh g}^{-1}$. (b) Coulombic efficiency of FSS-3, and the Cell-2 of FSS-3/G-15%.

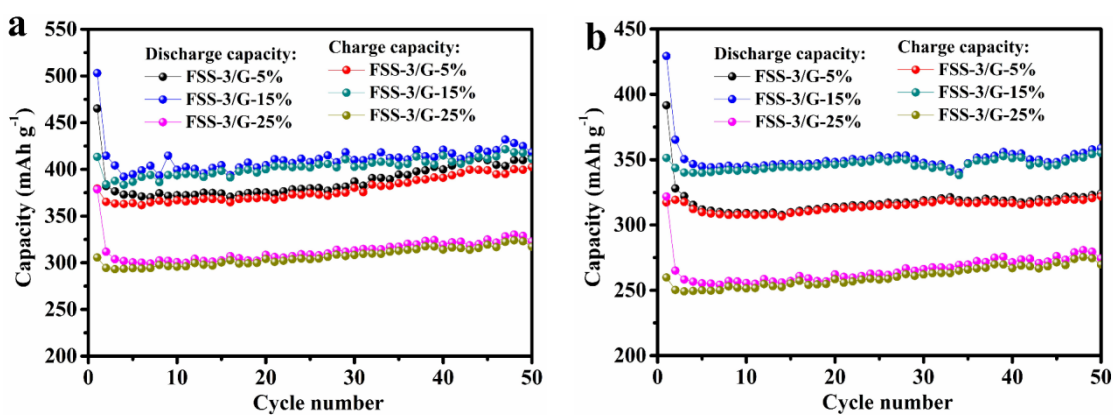


Fig. S12 (a) Galvanostatic discharge/charge cycling performance of FSS-3/G- $y\%$ ($y=5.0, 15.0, 25.0$) under 0.1 A g^{-1} , (b) Galvanostatic discharge/charge cycling performance of FSS-3/G- $y\%$ ($y=5.0, 15.0, 25.0$) under 1.0 A g^{-1} . The data of FSS-3/G-15% also shown in main text.

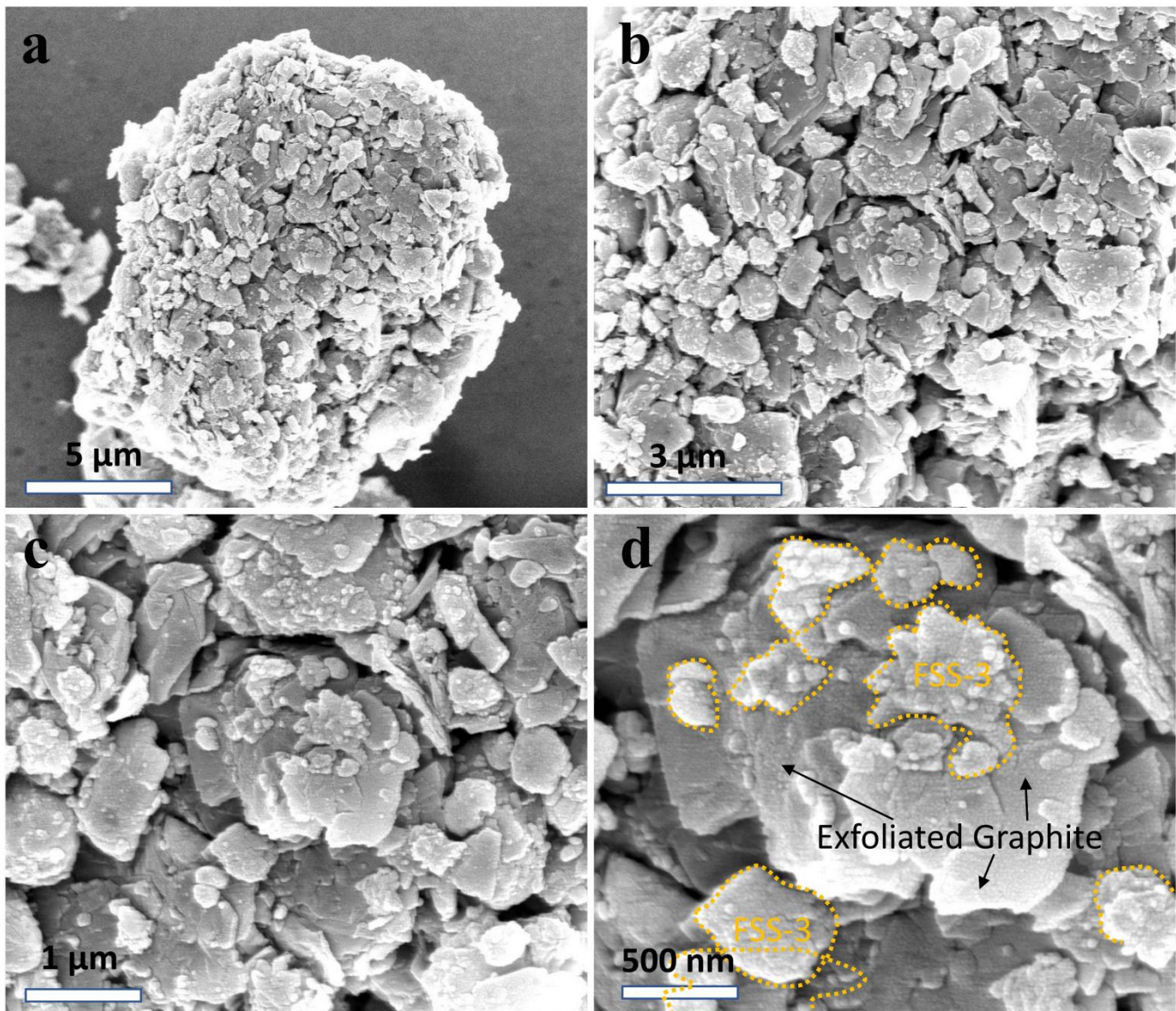


Fig. S13 (a-d) SEM images of FSS-3/G-15%.

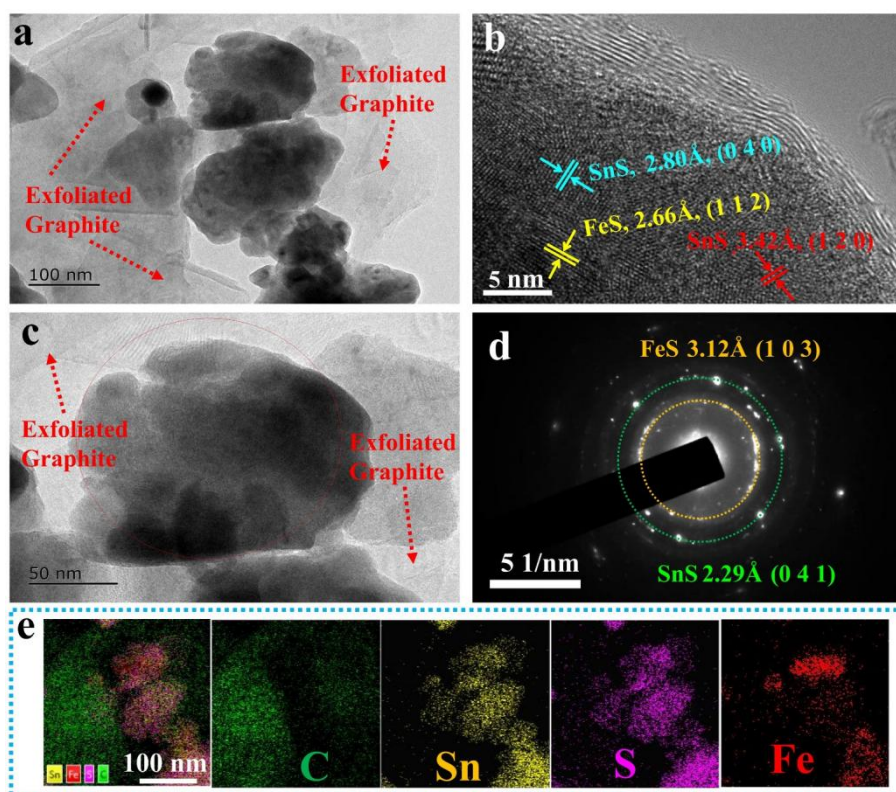


Fig. S14 (a-c) TEM images of FSS-1/G-15%, (d) SAED image of marked with red circles in figure c, (e) the C, Sn, S and Fe elements distribution of FSS-1/G-15%.

Fig. S14a and S14c depict FSS-1/G-15%, featuring particles firmly anchored onto exfoliated graphite, with particle sizes spanning from 50 to 500 nm. In the high-resolution image displayed in Fig. S14b, lattice fringes corresponding to the (0 4 0) plane of SnS with a fringe spacing of 2.80 Å, the (1 2 0) plane of SnS with a fringe spacing of 3.42 Å, and the (1 1 2) plane of FeS with a fringe spacing of 2.66 Å were observed. The selected area electron diffraction (SAED) pattern (Fig. S14d) allowed for the calibration of the (1 0 3) plane of FeS and the (0 4 1) plane of SnS. Elemental mapping analysis unveiled an uneven distribution of Sn and Fe, with Sn-enriched regions adjacent to Fe-sparse regions (Fig. S14e), providing further evidence of the presence of grain boundaries between SnS and FeS.

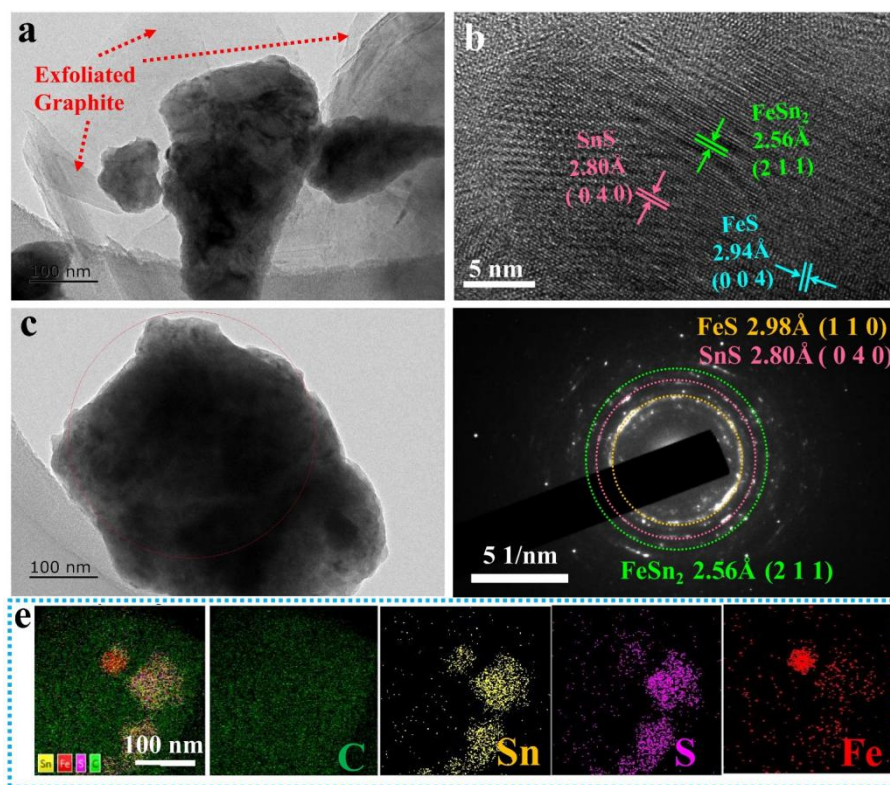


Fig. S15 (a-c) TEM images of FSS-2/G-15%, (d) SAED image of marked with red circles in figure c, (e) the C, Sn, S and Fe elements distribution of FSS-2/G-15%.

Fig. S15a and S15c depict FSS-2/G-15%, featuring particles firmly anchored onto exfoliated graphite, with particle sizes spanning from 50 to 500 nm. In the high-resolution image displayed in Fig. S15b, lattice fringes corresponding to the (0 4 0) plane of SnS with a fringe spacing of 2.80 Å, the (0 0 4) plane of FeS with a fringe spacing of 2.94 Å, and the (2 1 1) plane of FeSn₂ with a fringe spacing of 2.56 Å were observed. The selected area electron diffraction (SAED) pattern (Fig. S15d) allowed for the calibration of the (1 1 0) plane of FeS, (0 4 0) plane of SnS, and the (2 1 1) plane of FeSn₂. Elemental mapping analysis unveiled an uneven distribution of Sn and Fe, with Sn-enriched regions adjacent to Fe-sparse regions (Fig. S15e), providing further evidence of the presence of grain boundaries between SnS, FeS, and FeSn₂.

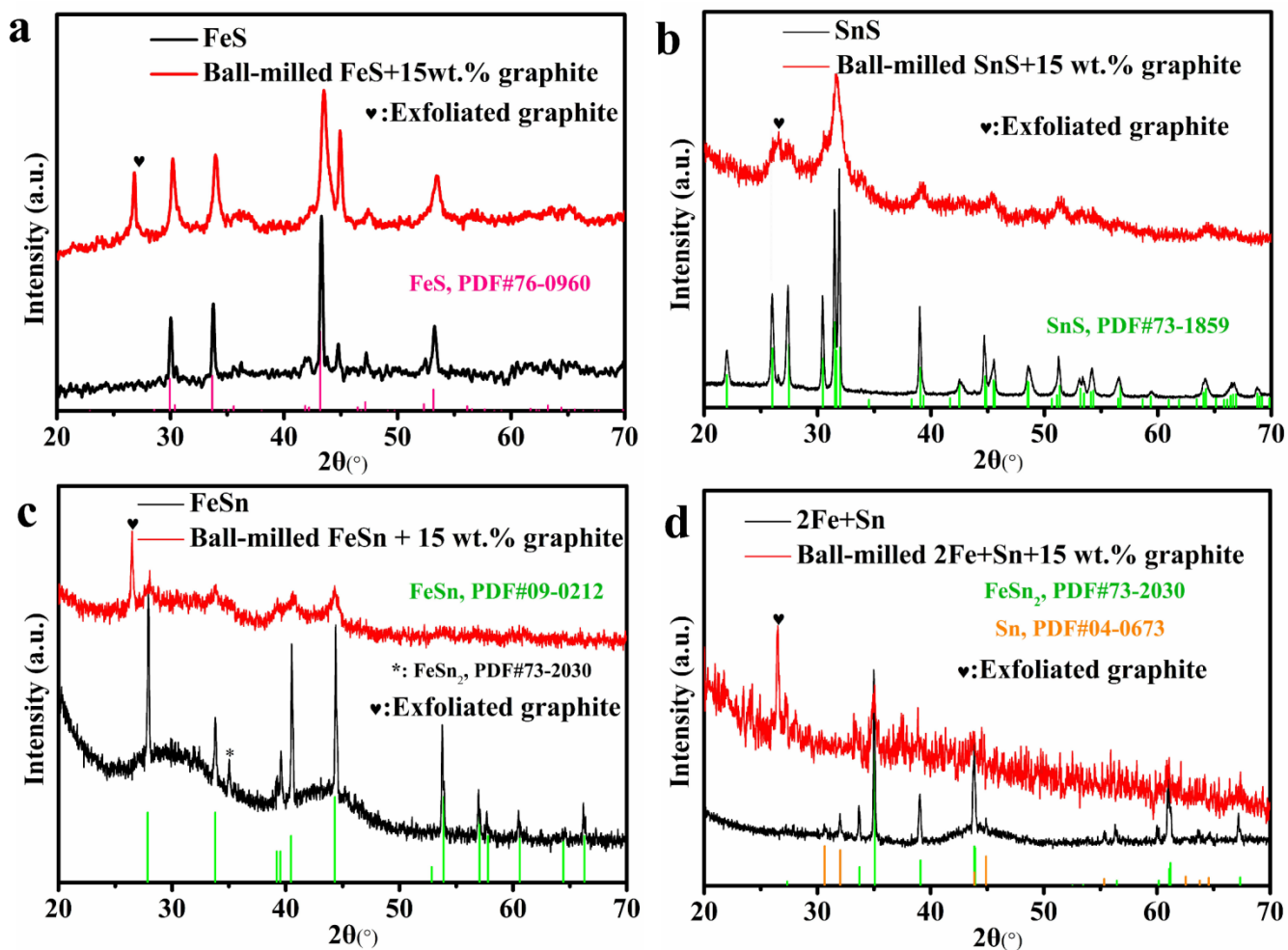


Fig. S16 (a) XRD curves of FeS and FeS/G-15%, (b) XRD curves of SnS and SnS/G-15%, (c) XRD curves of FeSn and FeSn/G-15%, (d) XRD curves of FeSn₂ and FeSn₂/G-15%. The graphite powder, FeS and SnS are supplied from Shanghai Aladdin Reagent Co., Ltd; the FeSn and FeSn₂ were synthesized by mixing the Fe and Sn powder in mole ratio of 1:1 and 1:2, then loaded into quartz tube, and heated 48 h at 600°C.

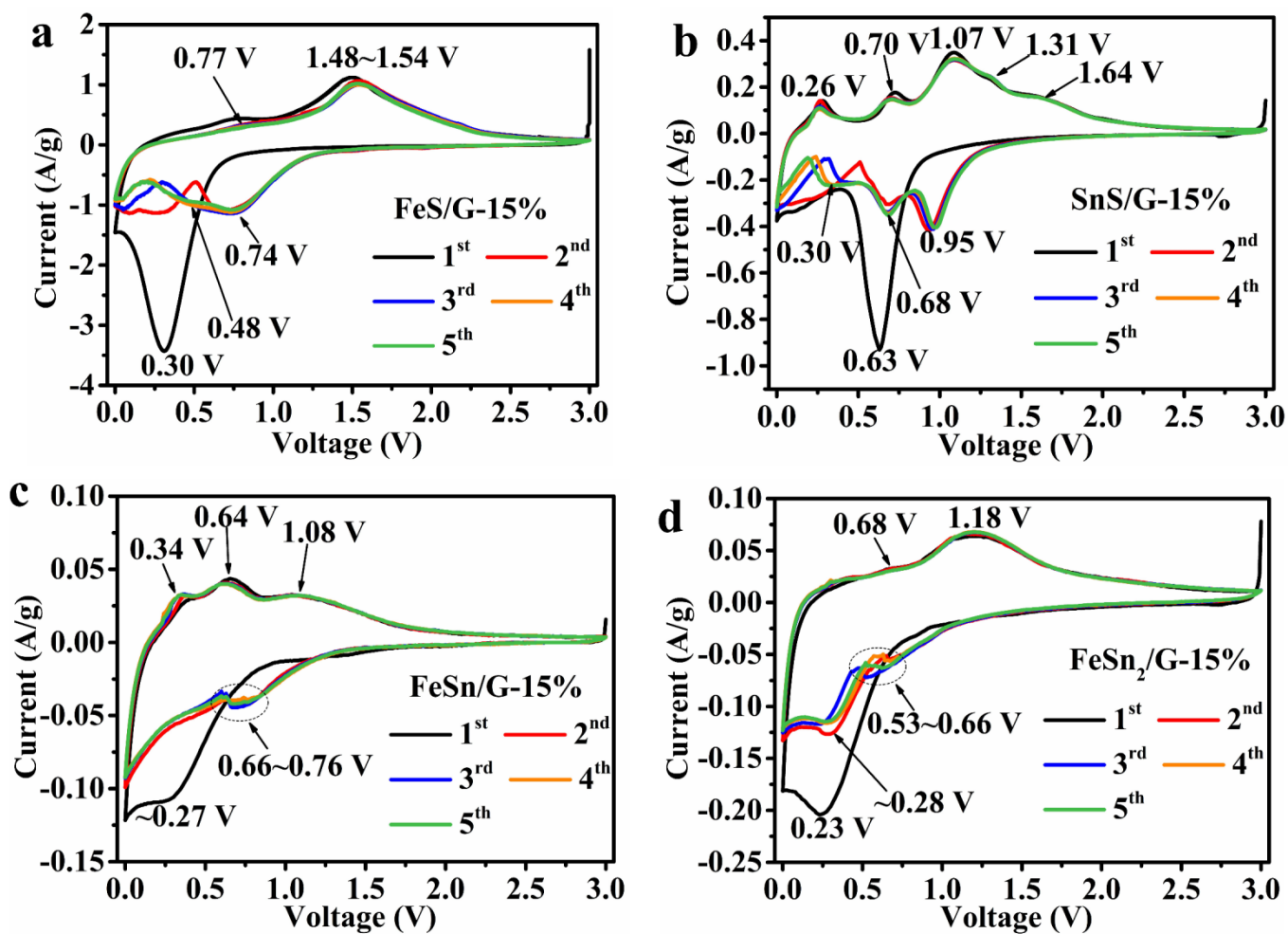


Fig. S17 (a) CV curves of FeS/G-15%, (b) CV curves of SnS/G-15%, (c) CV curves of FeSn/G-15%, (d) CV curves of FeSn₂/G-15%.

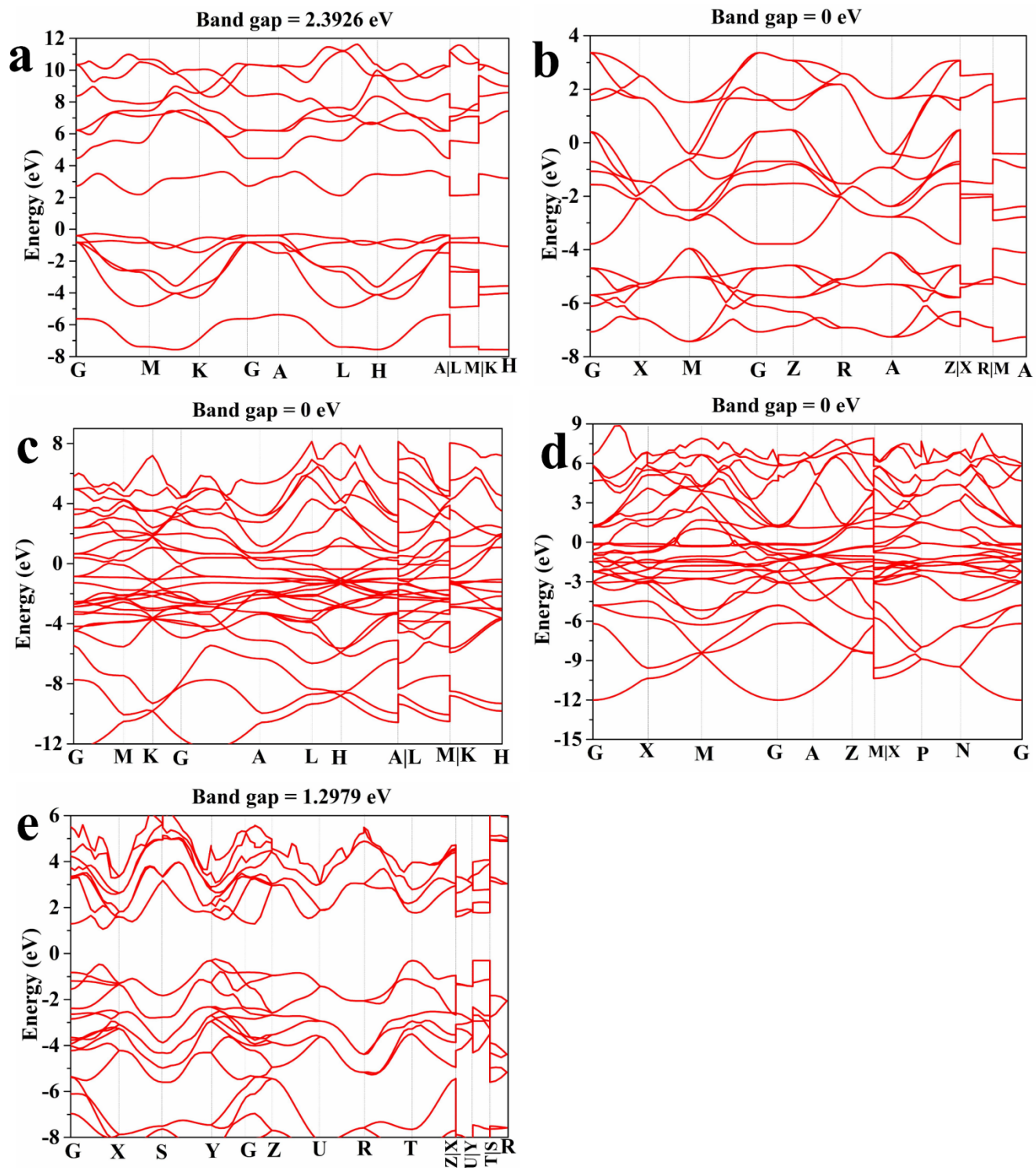


Fig. S18 (a) Band structure of SnS₂, (b) band structure of FeS, (c) band structure of FeSn₂, (d) band structure of FeSn, (e) band structure of SnS.

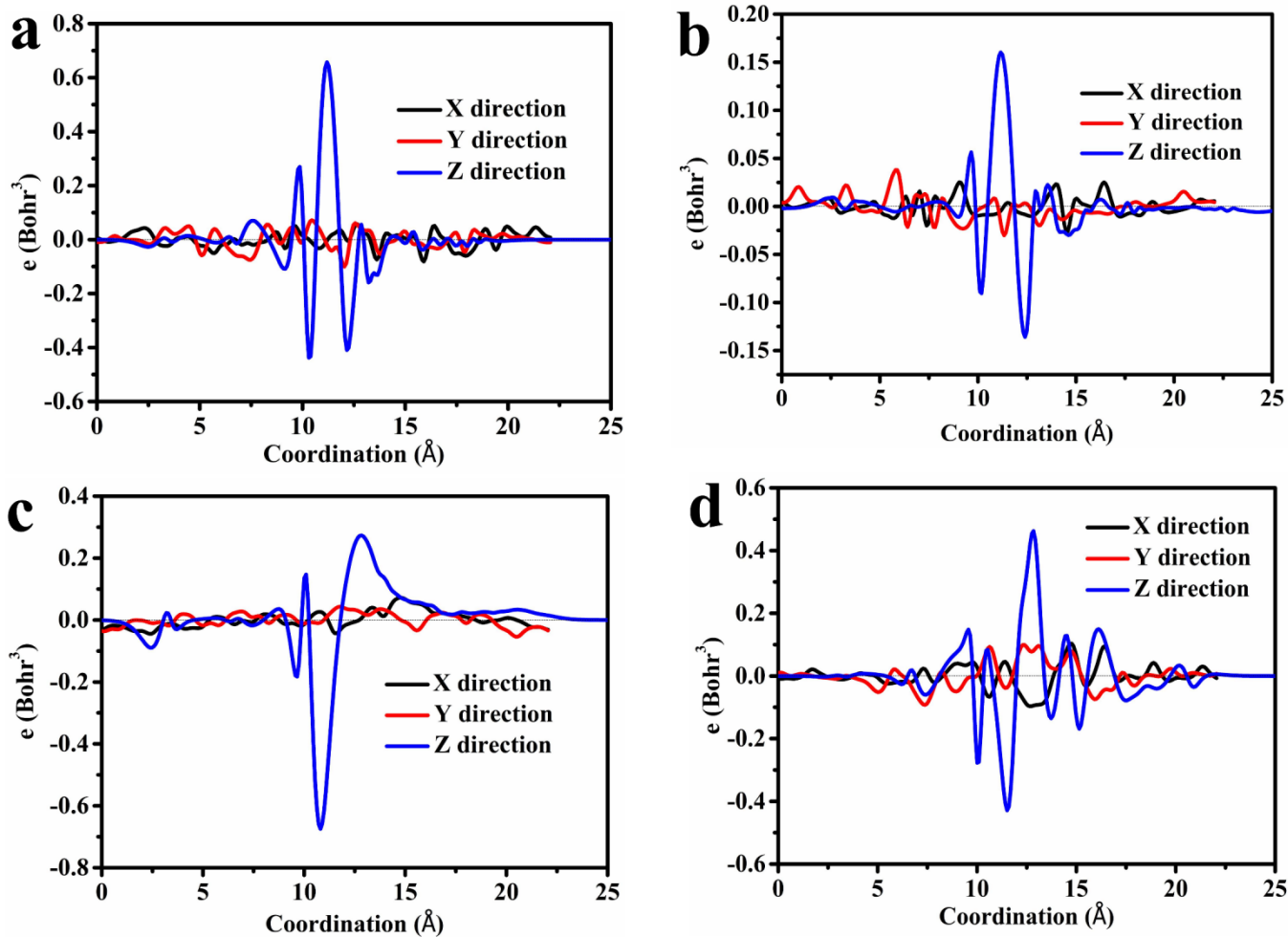


Fig. S19 (a) Electronic volatility of FeS/G, (b) electronic volatility of FeSn/G, (c) electronic volatility of FeSn₂/G, (d) electronic volatility of SnS/G.

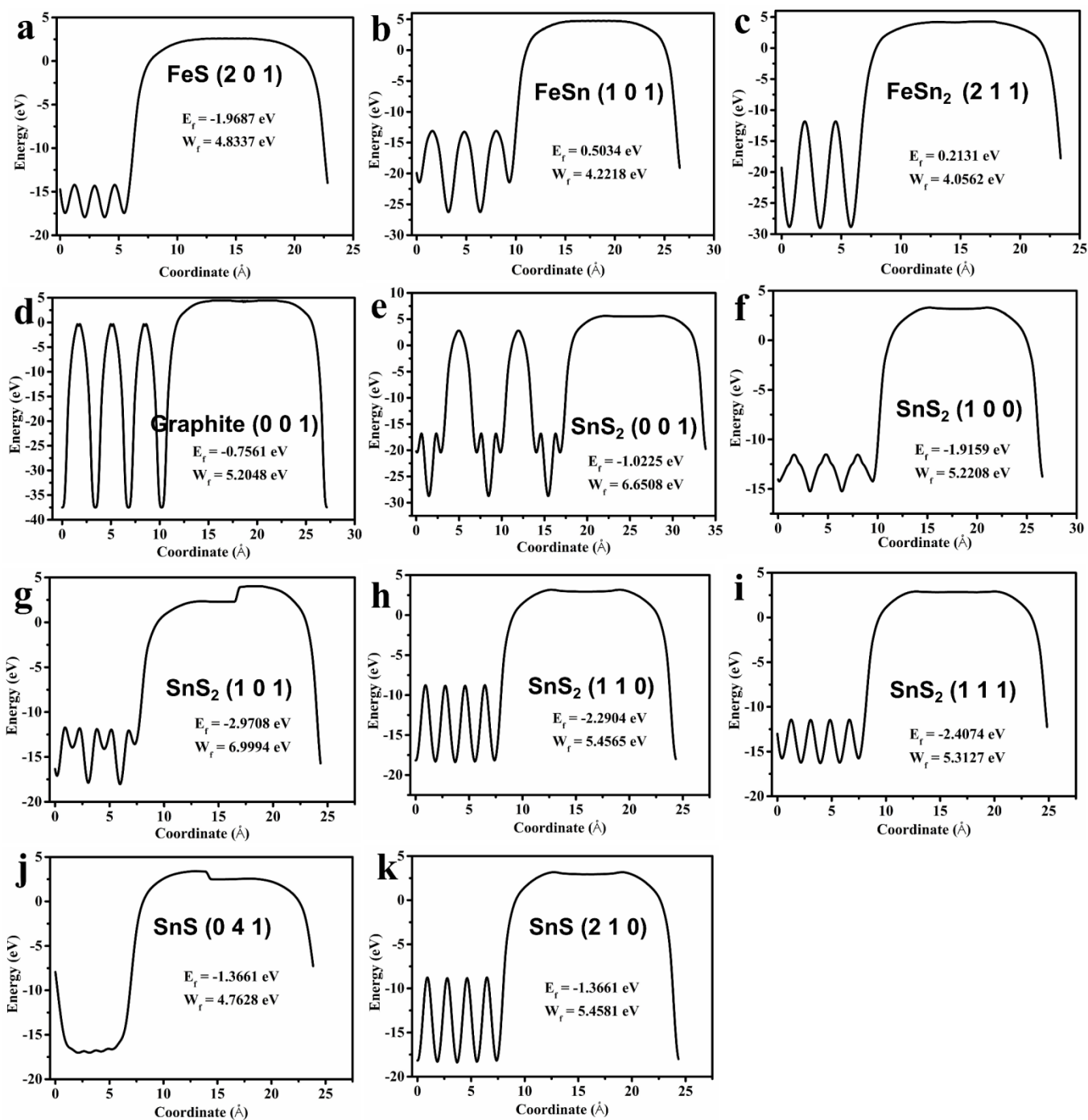


Fig. S20 Work functions of FeS, FeSn, FeSn₂, graphite, and SnS₂. (a) (2 0 1) plane of FeS, (b) (1 0 1) plane of FeSn, (c) (2 1 1) plane of FeSn₂, (d) (0 0 1) plane of graphite, (e) (0 0 1) plane of SnS₂, (f) (1 0 0) plane of SnS₂, (g) (1 0 1) plane of SnS₂, (h) (1 1 0) plane of SnS₂, (i) (1 1 1) plane of SnS₂, (j) (0 4 1) plane of SnS, (k) (2 1 0) plane of SnS.

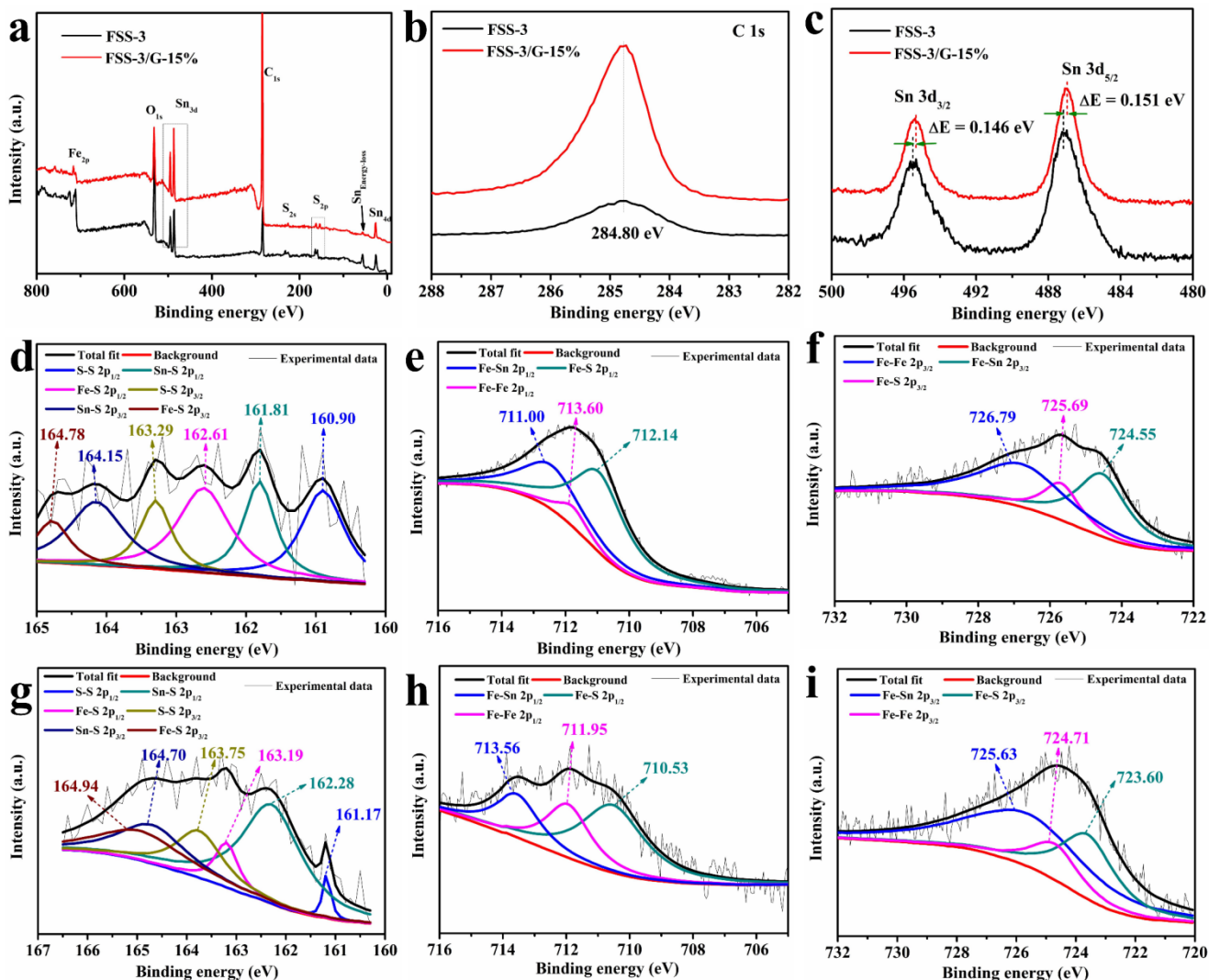


Fig. S21 The XPS spectra of FSS-3 and FSS-3/G-15%. (a) survey spectra, (b) C 1s spectra, (c) Sn 3d spectra, (d) S 2p spectra of FSS-3, (e) Fe 2p_{1/2} spectra of FSS-3, (f) Fe 2p_{3/2} spectra of FSS-3, (g) S 2p spectra of FSS-3/G-15%, (h) Fe 2p_{1/2} spectra of FSS-3/G-15%, (i) Fe 2p_{3/2} spectra of FSS-3/G-15%.

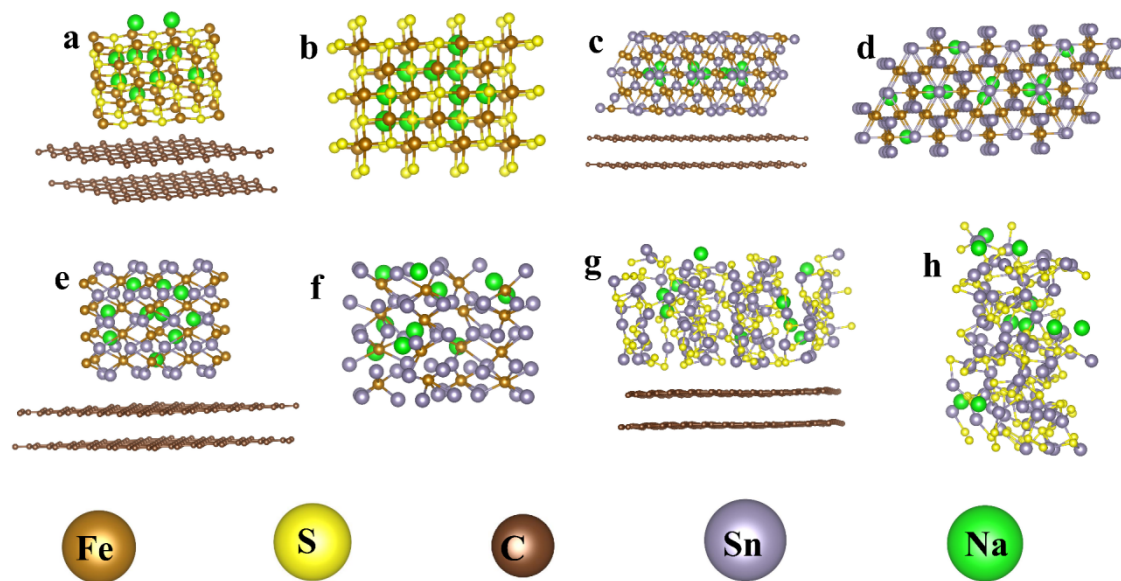


Fig. S22 The structs for the MD simulation. (a) Na/FeS/G, (b) Na/FeS, (c) Na/FeSn/G, (d) Na/FeSn, (e) Na/FeSn₂/G, (f) Na/FeSn₂, (g) Na/SnS/G, (h) Na/SnS.

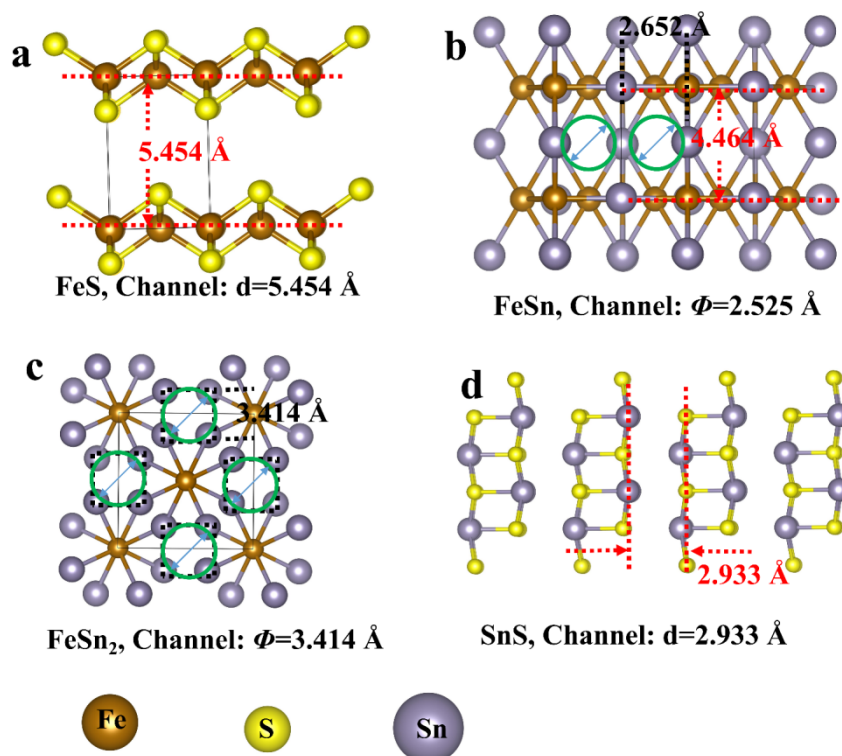


Fig. S23 The crystal structure analysis of the FeS (a), FeSn (b), FeSn₂ (c), and SnS (d).

References:

- [1] John, P., Perdew, Kieron, Burke, Matthias, Ernzerhof, Erratum, Generalized gradient approximation made simple, *Phys. Rev. Let.* (1996) 3865.
- [2] I.A.M. Ibrahim, Z. Lenčič, L. Benco, M. Hrabalová, P. Šajgalík, Cerium-doped LaSi_3N_5 : computed electronic structure and band gaps, *J. Eur. Ceram. Soc.* 34 (2014) 2705-2712.
- [3] Y.-Q. Xu, S.-Y. Wu, L.-J. Zhang, L.-N. Wu, C.-C. Ding, First-principles study of structural, electronic, elastic, and optical properties of cubic KNbO_3 and KTaO_3 crystals, *Phys. Status Solidi B* 254 (2017) e00644.
- [4] A. Ghysels, R.M. Venable, R.W. Pastor, G. Hummer, Position-dependent diffusion tensors in anisotropic media from simulation: oxygen transport in and through membranes, *J. Chem. Theory Comput.* 13 (2017) 2962-2976.
- [5] D.J. Brooks, B.V. Merinov, W.A. Goddard, B. Kozinsky, J. Mailoa, Atomistic description of ionic diffusion in PEO-LiTFSI: effect of temperature, molecular weight, and ionic concentration, *Macromolecules* 51 (2018) 8987-8995.
- [6] T. Ma, R. Jacobs, J. Booske, D. Morgan, Understanding the interplay of surface structure and work function in oxides: A case study on SrTiO_3 , *APL Mater.* 8 (2020) 071110.
- [7] Z. Ali, T. Tang, X. Huang, Y. Wang, M. Asif, Y. Hou, Cobalt selenide decorated carbon spheres for excellent cycling performance of sodium ion batteries, *Energy Storage Mater.* 13 (2018) 19-28.
- [8] D. Ledwoch, L. Komsysińska, E.M. Hammer, K. Smith, P.R. Shearing, D.J.L. Brett, E. Kendrick, Determining the electrochemical transport parameters of sodium-ions in hard carbon composite electrodes, *Electrochim. Acta* 401 (2022) 139481.